Damage Identification in Concrete using Impact Non-Linear Reverberation Spectroscopy

Article *in* NDT & E International · April 2015

DOI: 10.1016/j.ndteint.2015.04.002

3 authors, including:

Nils Ryden
Lund University
79 PUBLICATIONS **707** CITATIONS
SEE PROFILE

Andreas Jakobsson
Lund University
204 PUBLICATIONS **1,976** CITATIONS
SEE PROFILE

NDT&E International 75 (2015) 15–25

Contents lists available at ScienceDirect

NDT&E International

journal homepage: www.elsevier.com/locate/ndteint

Damage identification in concrete using impact non-linear reverberation spectroscopy

Unn Dahlen [a,*], Nils Ryden [b], Andreas Jakobsson [a]

[a] Department of Mathematical Statistics, Lund University, Sweden
[b] Division of Engineering Geology, Lund University, Sweden

ARTICLE INFO

Article history:
Received 15 December 2014
Received in revised form
7 April 2015
Accepted 10 April 2015
Available online 23 April 2015

Keywords:
Non-destructive testing
Impact method
Reverberation spectroscopy

ABSTRACT

High amplitude non-linear acoustic methods have shown potential for the identification of micro damage in brittle materials such as concrete. Commonly, these methods evaluate a non-linearity parameter from the relative change in frequency and attenuation with strain amplitude. Here, a novel attenuation model is introduced to describe the free reverberation from a standard impact resonance frequency test, together with an algorithm for estimating the unknown model coefficients. The non-linear variation can hereby by analyzed over a wider dynamic range as compared to conventional methods. The experimental measurement is simple and fully compatible with the standardized free-free linear impact frequency test.

1. Introduction

The development of non-destructive testing techniques to detect early micro-cracks or imperfections in construction materials is important for efficient maintenance and management of existing infrastructure. During recent years, non-linear non-destructive methods have attracted notable interest, and have been proved to be more sensitive to the detection of damage in, for example, concrete, as compared to traditional linear acoustic methods [1]. When quasi-brittle materials such as concrete are damaged (micro-cracked), enhanced non-linear effects arise in the acoustic wave propagation characteristics [2]. Some typical non-linear manifestations in resonance frequency testing are the downward shift of the frequency and the increase in attenuation with increasing amplitudes (fast dynamics) [3–5]. The logarithmic recovery of this frequency shift with time after a stress or temperature disturbance may also be studied (slow dynamics) [6–8]. Furthermore, non-linear characteristics can be revealed by studying the behavior of higher harmonics and interference (modulation) between different frequencies [9,10]. Although many different methods have been proposed (see, e.g., [11]), there is still a need for practical and simple methods similar to the standardized linear resonance frequency testing techniques widely used today [12,13]. Non-linear ultrasound spectroscopy (NRUS) techniques are based on the measurement of resonance frequencies at different amplitudes and have shown promising results for the detection of distributed damage in concrete [14,15,3,16]. These methods can sense a large volume of a micro-cracked sample and are not too sensitive to the position of the sensors [17]. In the single-mode resonance spectroscopy (SIMONRAS) technique, the output vibration amplitude is measured while sweeping over an interval comprising a resonance frequency. The relative frequency and attenuation shift as a function of the excitation amplitude is studied and therefore several frequency sweeps with different input forces are acquired in order to evaluate the relative non-linearity parameter. Additionally, the frequency is swept very slowly to guarantee steady state response [18], making these methods both time consuming and practically cumbersome.

A faster variant of the NRUS method is the non-linear impact resonance spectroscopy (NIRAS) method, which was demonstrated on concrete by Chen et al. [19,20], Lesnicki et al. [14,21], Bouchaala et al. [22], and Eiras et al. [23]. The NIRAS technique relies on an impulse excitation of the specimen which is repeated with different impact strengths. This measurement set-up is easily performed and similar to the standardized free–free resonance test for concrete [13]. The relative frequency shift is then studied in the frequency domain by analyzing the peak amplitude and resonance frequency of one mode from multiple impacts with different strength. A practical advantage with impact resonance methods is that a wide frequency range including multiple resonance modes can be covered in a simple test [12,24,25] (in conventional NRUS, based on frequency sweep measurements, the source and experimental set-up needs to be tuned to the frequency of interest). However, a current limitation with the NIRAS method is that the extracted amplitude from each impact is not exactly related to the true physical amplitude in the sample. In

* Corresponding author.
E-mail address: unn@maths.lth.se (U. Dahlen).

http://dx.doi.org/10.1016/j.ndteint.2015.04.002
0963-8695/

order to move towards quantitative non-linear measurements, it is important to use the physical amplitude in the sample [26]. In the NIRAS method, the extracted peak amplitude is formed as a weighted average of the frequency- and amplitude-content in the complete (naturally damped) signal. This analysis procedure, based on the Fourier transform of each signal, results in a relatively limited dynamic range over which the frequency shift may be evaluated. The measurable dynamic range from the smallest to the largest amplitude peak is typically only about a factor 8 in the frequency domain, although each time domain signal may have a dynamic range of at least a factor 100 [19,14,22,5]. Furthermore, it should be noted that in a non-linear reverberation signal, wherein both the frequency and the attenuation change as a function of time and amplitude, both these factors will influence the width and the amplitude of the resulting resonant spectral peak [1]. The true physical amplitude and amplitude range in the sample is thus partially masked when the complete length of the signal is analyzed with a Fourier transform [27].

The non-linear reverberation spectroscopy (NRS) method introduced by Van Den Abeele et al. [1,28] instead exploits the natural reverberation of a non-linear signal in the time domain. This is done by exciting a resonance frequency of a sample with a loudspeaker source, and then utilizing the natural decay in the reverberation of the response after the loudspeaker is turned off. The non-linear parameter is evaluated by analyzing the change in the frequency and the attenuation as the signal is naturally decaying. The reverberation signal is divided into multiple small time windows, of about 20 cycles, and an exponentially decaying sine function with a constant damping and frequency parameter is fitted to each time window [28], i.e., the kth window of the (noiseless) signal, x_t, may be modeled as

$$x_k(t) = A_k e^{-\alpha_k t} \sin(2\pi f_k t + \phi_k) \tag{1}$$

where A_k, α_k, f_k, and ϕ_k denote the amplitude, attenuation, frequency, and the phase, respectively. As the sample is excited using only a single resonance frequency, the simple signal model in (1) may be used to represent the measured signal within each time window. As for the NIRAS method, the extracted amplitude is here a weighted average of the amplitude within each time window, and thus, it does not correspond to the true physical instantaneous amplitude at any specific time. For larger and heavier concrete type of samples, the continuous excitation of large vibration amplitudes with a loudspeaker or shaker can be difficult to achieve, and, as a result, limiting the measured dynamic range [1].

A simple impact hammer is usually preferred in resonance frequency testing of concrete samples [13,25]. In contrast to the single frequency source, an impact source generates a wide range of frequencies, and as a result the measured response usually contains multiple modes of vibration, making the single mode NRS analysis more difficult to apply directly to larger concrete samples. An impact-based version of the NRS technique was recently introduced by Eiras et al. [5]. In this work, the reverberation from a standard impact resonance frequency test (see, e.g. [13]) was analyzed using a short time Fourier transform (spectrogram), and the non-linear frequency shift as a function of amplitude was successfully extracted over a dynamic range of a factor 6 (in the frequency domain). The method is practical and fast, but suffers from the same smearing of the true physical instantaneous amplitude in the sample as the NIRAS and NRS methods.

In this study, we investigate a novel method of characterizing the extent of damage in a concrete specimen. The proposed technique, called "Impact Non-linear reverberation spectroscopy" (INRS), is based on a combination of the existing NIRAS and NRS techniques, but as for the spectrogram-based technique recently introduced in [5], the proposed method only requires a single impact excitation to allow for a reliable estimate of the non-linearity, although our approach allows for an estimate over a notably wider dynamic range. This is achieved by a combination of the use of a detailed *parametric* signal model as well as a robust iterative parameter estimation technique that estimates the parameters detailing each of the signal modes separately. This allows the continuous instantaneous true amplitude, frequency, and damping of each mode to be characterized as a function of time, allowing for detailed information of the non-linear parameters. By stochastic modeling of the reverberation signal after a single impulse excitation of the specimen, we aim to find parameters of the non-linearity, which may be associated with the degree of damage in the material. This method has the potential of allowing for fast and accurate operational measurements over a wide amplitude range, as well as enabling the phase and amplitude part of the signal to be studied separately. The proposed parametric model and estimation algorithm is described in detail along with an evaluation of the model using experimental data at three different levels of damage. Results indicate that the non-linear effect on both the frequency and the attenuation may be extracted over a relatively wider amplitude range as compared to the traditional NIRAS and NRS techniques, and this from the response of only a single impact. In this study, the results are restricted to the strongest measured resonance mode, although multiple modes may be studied simultaneously in a similar manner, potentially offering further information of the non-linearities of the material. Similar to the method by Eiras et al. [5], the non-linear parameters may in our setup be obtained in addition to the linear elastic constants using the same simple and standardized free–free resonant test normally conducted on concrete, stabilized soil, or other construction materials [13,24,25].

The remainder of the paper is organized as follows: in the following section, we briefly review the theoretical background of the non-linear measurements. Then, in Section 3, we discuss the experimental setup and the resulting data sets. In Section 4, we introduce the suggested signal model and the proposed parametric estimation algorithm. In Section 5, we evaluate the proposed model and the estimation algorithm using measured impact responses from concrete, showing both that the model well describes the data and that the algorithm is able to accurately estimate the unknown parameters. Finally, in Section 7, we conclude on the work.

2. Theoretical background

When concrete and other heterogeneous mesoscopic elastic materials are damaged, naturally occurring non-linear *hysteretic* effects increase [2,9]. The classical theory of non-linear atomic elasticity does not apply for mesoscopic hysteretic materials, such as concrete. In addition to the classical non-linearity stress–strain relation, one then also has to take account for hysteresis and discrete memory. The phenomenological model presented in [9] expresses the relation between the stress, σ, and the strain, ϵ, in one dimension as

$$\sigma = \int E(\epsilon, \dot{\epsilon})\, d\epsilon \tag{2}$$

where E is the non-linear hysteretic modulus

$$E = E_0[1 + \beta\epsilon + \delta\epsilon^2 + \alpha(\Delta\epsilon + \epsilon\ \mathrm{sgn}(\dot{\epsilon}))] \tag{3}$$

with E_0 denoting the linear modulus, β and δ the classical quadratic and cubic non-linear parameters, respectively, ϵ the

strain, $\Delta\epsilon$ the strain amplitude in a cycle, $\dot{\epsilon}$ the strain rate, and

$$\mathrm{sgn}(\dot{\epsilon}) = \begin{cases} 1, & \dot{\epsilon} > 0 \\ -1, & \dot{\epsilon} < 0 \\ 0, & \dot{\epsilon} = 0 \end{cases} \quad (4)$$

and where the parameter α is a measure of the hysteresis of the material. Two of the main manifestations of the non-linear hysteresis properties of a material are the downward shift of the resonance frequency and the increasing attenuation factor (damping factor) with increasing excitation amplitude. These non-linear effects are more evident for larger excitation amplitudes (see, e.g., [18]). Studies of the frequency shift as a function of the amplitude has shown the existence of a quadratic dependence [29–31,27]. However, in many experimental studies, a linear approximation between the frequency shift and the amplitude has been successfully used over a limited amplitude range [9,19,14,16,23]. Commonly, the linear frequency shift with strain amplitude is given as

$$\frac{f_0 - f}{f_0} = c_1 \Delta\epsilon \quad (5)$$

where f_0 is the linear resonance frequency at the smallest measurable strain level, and f the resonance frequency at the increasing excitation amplitude. Furthermore, the increase of modal damping ratio with increasing strain amplitude may be expressed as

$$\frac{\xi - \xi_0}{\xi_0} = c_2 \Delta\epsilon \quad (6)$$

where ξ_0 is the modal damping ratio at low excitation amplitude, and ξ is the damping at increasing drive amplitude. The coefficients c_1 and c_2 are both proportional to the hysteresis parameter, α. Thus, by studying the relative change of the frequency and the attenuation, one may obtain information about the extent of damage in the examined concrete. This procedure forms the basis of the NRUS technique. Recently, Payan et al. [26] emphasized the importance of using the true physical amplitude (strain level) to estimate absolute values of c_1 and c_2 towards real quantitative measurements of damage in concrete.

3. Experimental setup

The studied experimental setup is shown in Fig. 1, illustrating how the examined specimen is placed on a soft foam to allow for free vibrations, and how a small hammer is used to excite the sample. In our experiments, we examine the impact responses of a sample disc of progressively damaged concrete, as well as a steel rod, which is used as a reference sample. The length, L, the diameter, D, the approximated linear modulus, E, Poisson's ratio, and the density of the samples are given in Table 1. The vibration response is initialized by a small impactor positioned at the center of the specimen. This set-up will primarily excite the fundamental radially symmetric longitudinal mode, $f_{(0,1)}$, where the indices represent the number of nodal diameters and circles in the mode shape (see e.g., [32], p. 258–69). Although we aim to only excite one resonance frequency, responses from other modes are unavoidable. In the following modeling, we will therefore also take two further vibrational modes into account, namely the fundamental mode, $f_{(2,1)}$, and the first higher radially anti-symmetric flexural mode, $f_{(3,1)}$.

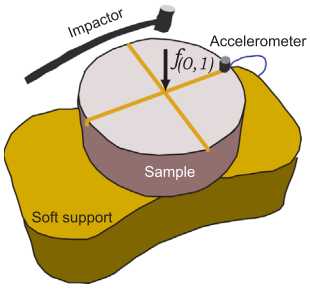

Fig. 1. Experimental setup.

An illustration of the mode shape of $f_{(0,1)}$ is given in Fig. 2, wherein the normalized acceleration in z-direction is displayed. This plot has been obtained using the Comsol software [33], which numerically calculates the resonance frequencies of a free sample with specified geometry and material properties. The input values were manually tuned to fit the experimental results obtained from the impact method, by observing the real resonance modes. In this Comsol model, the volumetric strain is approximately of an order 10^{-9} of the acceleration in the concrete sample at this frequency. This constant can be used to estimate the volumetric strain level in the studied sample at this particular resonance frequency, i.e., $f_{(0,1)}$, from the measured acceleration in the z-direction [26]. The vibration response of the specimen is measured with a miniature accelerometer (PCB model 352B10 with a weight of 0.7 g) positioned at the edge of the disc, as may also be seen in Fig. 1. The signal was fed through a signal conditioner (PCB model 480B21) and a data acquisition device (NI-USB-6251) before being saved. The free vibration response is collected by inducing an impact force in the center of the specimen with a small impactor consisting of a screw (4 g) attached to a plastic cable tie (Fig. 1). Multiple impacts were recorded in order to check the repeatability of the method. The studied 20 mm thick concrete disk was sawed out from a longer 200 mm concrete cylinder of C20/25 concrete (characteristic cylinder and cube strength of 20 and 25 MPa, respectively). The several years old concrete had a natural and relatively low damage level. In subsequent measurements, the damage level was then successively increased by inducing invisible micro-cracks by hitting the center of the specimen with a

Table 1
Geometry and approximate linear elastic properties of the tested samples.

Sample properties	Damaged concrete	Structural steel
Length	20 mm	550 mm
Diameter	100 mm	30 mm
E-modulus	≈ 33 GPa	≈ 210 GPa
Poisson's ratio	0.18	0.30
Density	2400 kg/m^3	7800 kg/m^3

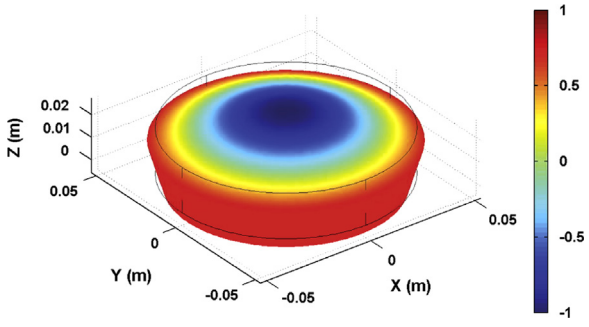

Fig. 2. Mode shape of the fundamental radially symmetric mode ($f_{(0,1)}$) with eigenfrequency = 10,128 Hz color coded with respect to normalized acceleration in the z-direction. (For interpretation of the references to color in this figure caption, the reader is referred to the web version of this paper.)

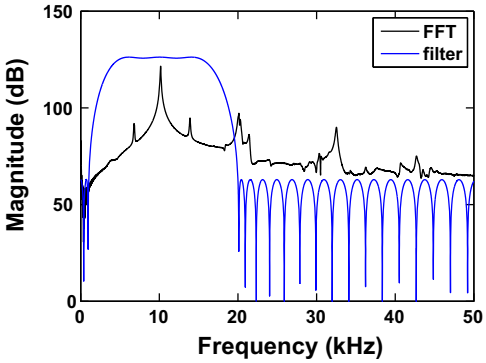

Fig. 3. The spectral content of the vibration response, showing the three main extracting modes of the signal, $f_{(2,1)}$, $f_{(0,1)}$, and $f_{(3,1)}$, together with the (scaled) frequency response of the applied bandpass filter.

larger instrumented hammer (PCB model 086D05 with a weight of 0.32 kg), as demonstrated by Van Den Abeele et al. [3]. The damage force pulse was also recorded and had a pulse length of 0.3 ms and a peak force of 2000 N. Ten measurements with the small impact source were recorded for each of the three examined damaged levels, $D=1$, 2, and 3. Temperature and humidity were kept constant during the entire test, which lasted for about 15 min. As a reference, the longitudinal free vibration response was also collected from the undamaged steel rod (Table 1) in a similar fashion, using the same equipment. The steel rod was placed on soft foam and excited in longitudinal mode with the accelerometer attached in one end while impacting the sample in the center of the opposite end [13].

The sampling interval, d_t, of the free vibrational response was $d_t = 2\times 10^{-6}$ s, yielding the Nyquist frequency $f_N = 1/(2d_t) = 250$ kHz. The total sampling time needed for capture the entire signal decay was approximately 0.025 s for the concrete specimen, and 1 s for the steel rod. This correspond to 10,250 samples for each concrete measurement and 500,000 samples for each steel measurement.

Fig. 3 shows the spectral content of the signal, as estimated using the magnitude squared Fast Fourier Transform (FFT), evaluated over 100,000 frequency grid points. The three excited vibrational modes $f_{(2,1)}$, $f_{(0,1)}$, and $f_{(3,1)}$ are located at approximately 7, 10, and 14 kHz, respectively. It is worth noting that additional higher modes of vibration and possible non-linear harmonics of the fundamental modes can be observed at higher frequencies. In order to reduce the influence of such disturbances, we introduce a bandpass filter retaining only the frequency region of interest. The (scaled) frequency response of the used filter is also illustrated in the figure (see also [34], p. 31–4). This filter is designed to also remove low frequencies, in order to reduce leakage from low-frequency negative frequencies in the later used wall filter, as discussed further below.

4. Proposed method

In order to accurately determine the characteristics of the excited modes, we introduce a detailed parametric signal model, consisting of the response of each of the d excited modes. As noted, earlier works have shown that one may, for non-linear materials, expect a frequency increase coupled with a decreasing attenuation as the amplitude of the reverberation signal decreases over time [30,31,27,5]. In order to allow for such dependencies, we here model each of the vibrational modes as an exponentially damped *complex-valued* signal with a polynomial phase and attenuation, such that the kth order mode may be expressed as

$$z_k(t,\boldsymbol{\theta}_k) = \rho_k e^{-\psi(t,\boldsymbol{\theta}_k)+i\phi(t,\boldsymbol{\theta}_k)} \tag{7}$$

for $t=1,\ldots,T$, where T is the number of samples, and where ρ_k, $\psi(t,\boldsymbol{\theta}_k)$, and $\phi(t,\boldsymbol{\theta}_k)$ denote the amplitude, attenuation, and phase of the signal, respectively, with $\boldsymbol{\theta}_k$ denoting the parameters detailing the mode (as detailed below). Here, the attenuation and the phase are modeled as polynomials of order P_k and Q_k, respectively, such that

$$\psi(t,\boldsymbol{\theta}_k) = \sum_{m=1}^{P_k} b_m t^m \tag{8}$$

$$\phi(t,\boldsymbol{\theta}_k) = \sum_{m=0}^{Q_k} a_m t^m \tag{9}$$

with b_m and a_m denoting the mth coefficient in the attenuation and phase polynomials, respectively. Gathering the polynomial coefficients, the unknown parameters for the kth mode may thus be expressed as

$$\boldsymbol{\theta}_k = [\rho_k \;\; b_{1,k} \;\; \ldots \;\; b_{P_k,k} \;\; a_{0,k} \;\; \ldots \;\; a_{Q_k,k}]^T \tag{10}$$

It is worth noting that the commonly used exponential decay is here thus replaced by the polynomial decay in (8), thereby allowing also for higher order decays. Note also that by using the parametric model, we may analyze the non-linear variation in frequency and attenuation over the entire dynamic range of the time domain signal. The increased dynamic range is obtained by utilizing the known gradual and smooth nature of the non-linear shift as a function of the amplitude (see also [27]). The proposed model thus generalizes on earlier studies where both linear and quadratic frequency dependent strain amplitude dependences have been proposed; the model both allows the modes to scale linearly with acceleration for a constant frequency, as well as the frequency and attenuation to vary over time and amplitude. By combining the complex-valued modes detailing the corresponding positive and negative frequencies, one thus obtains the resulting real-valued mode. As a result, the measured (real-valued) vibrational response signal may be well modeled as the contribution from both the d positive and the d negative frequency modes, i.e.

$$x_R(t) = \sum_{k=1}^{2d} z_k(t,\boldsymbol{\theta}_k) + u_R(t) \tag{11}$$

where $u_R(t)$ denotes an additive (real-valued) corrupting noise, here assumed to be well modeled as a zero-mean white Gaussian noise. Clearly, the positive and negative modes contain redundant information, and the complexity of the model may therefore be reduced by retaining only either the positive or the negative component of each mode. This may be done without loss of information by forming the discrete-time analytical signal of $x_R(t)$, using the discrete-time Hilbert transform (see also [35]), which functions as a wall filter retaining only the positive frequencies of the signal (which are scaled by a factor two to retain the total signal power). The discrete-time analytical signal thereby yields a complex-valued signal representation containing only the d positive frequency modes, i.e.

$$x(t) = \sum_{k=1}^{d} z_k(t,\boldsymbol{\theta}_k) + u(t) \tag{12}$$

for $t=1,\ldots,T$, where $u(t)$ is the corresponding complex-valued noise term. Hence, by modeling the complex-valued signal, we have reduced the computational complexity to the estimation of d frequency components compared to $2d$ frequency components contained in the real-valued signal.

Algorithm 1. The proposed INRS algorithm, Part 1.

for $\ell = 1$ **to** d **do**
  iter $= 1$
  while iter $<$ IterMax $\wedge$ $r > \epsilon_1$ **do**
    Form $x_l(t,l)$ and use it to estimate $\hat{\boldsymbol{\theta}}_{y,l}^{\text{iter}}$.[1]
    for $j = 1$ **to** $\ell - 1$ **do**
      Form $x_l(t,j)$ and use it to estimate $\hat{\boldsymbol{\theta}}_{y,j}^{\text{iter}}$.
    end for
    Calculate the residual: $r_{\text{iter}} = x(t) - \sum_{k=1}^{\ell} y_0(t, \hat{\boldsymbol{\theta}}_{y,k}^{\text{iter}})$
    Form the residual norm: $r = \frac{|\, \|r_{\text{iter}-1}\| - \|r_{\text{iter}}\| \,|}{\|r_{\text{iter}-1}\|}$
    iter $=$ iter $+ 1$
  end while
  if $|a_{k_1,1} - a_{k_2,1}| < \epsilon_2,\ \{(k_1,k_2) : k_1, k_2 \in \{1:\ell\}, k_1 \neq k_2\}$ **or** $a_{k_1,1} < \epsilon_3,\ \forall k_1 \in \{1:\ell\}$ **then**
    $d = l - 1$
    return
  end if
end for
Global optimization

$$\{\hat{\boldsymbol{\theta}}_{y,k=1:d}\} = \arg \min_{\{\boldsymbol{\theta}_{y,k=1:d}\}} \sum_{t=1}^{T} \left| x(t) - \sum_{k=1}^{d} y_0(t, \hat{\boldsymbol{\theta}}_{y,k}) \right|^2$$

Using the proposed signal model, one may form a least-squares (LS) estimate of all the unknown parameters by minimizing

$$\boldsymbol{\theta} = \arg \min_{\boldsymbol{\theta}} \sum_{t=1}^{T} \left| x(t) - \sum_{k=1}^{d} z_k(t, \boldsymbol{\theta}_k) \right|^2 \tag{13}$$

Algorithm 2. The proposed INRS algorithm, Part 2.

Require: $\hat{\boldsymbol{\theta}} = \{\hat{\boldsymbol{\theta}}_{y,k=1:d}\}$ from Algorithm 1.
for $\ell = 1$ **to** d **do**
  $j = 2$
  while $P_\ell \geq j$ **do**
    Initialize the LS optimization with $\boldsymbol{\theta}_0 = [\hat{\boldsymbol{\theta}}\ b_{j,\ell}]$, with $b_{j,\ell} = 0$
    Estimate

$$\hat{b}_{1:j,\ell} = \arg \min_{b_{1:j,\ell}} \sum_{t=1}^{T} \left| x(t) - \sum_{k=1}^{d} z_k(t, {}^{2}\hat{\boldsymbol{\theta}}_{k,\ell}) \right|^2$$

    Update the estimated parameter set

$$\hat{\boldsymbol{\theta}} = [\hat{\boldsymbol{\theta}}_{-b_{1:j,\ell}}\ \hat{b}_{1:j,\ell}]$$

    $j = j + 1$
  end while
end for
Global optimization

$$\hat{\boldsymbol{\theta}} = \arg \min_{\boldsymbol{\theta}} \sum_{t=1}^{T} \left| x(t) - \sum_{k=1}^{d} z(t, \hat{\boldsymbol{\theta}}_k) \right|^2$$

[1] $\hat{\boldsymbol{\theta}}_{y,l}^{\text{iter}}$ is the estimate of the parameter set $\boldsymbol{\theta}_y$, see Eq. (18), for mode ℓ, at iteration step iter.

[2] Here, the parameter set $\hat{\boldsymbol{\theta}}_{k,\ell}$ is fixed for $k \neq \ell$, with $\hat{\boldsymbol{\theta}}_{k,\ell} = \{\hat{\boldsymbol{\theta}}_{y,k}, b_{2:P_k,k}\}$ for $k < \ell$, and $\hat{\boldsymbol{\theta}}_{k,\ell} = \hat{\boldsymbol{\theta}}_{y,k}$ for $k > \ell$. For $k = \ell$, we have that $\hat{\boldsymbol{\theta}}_{k,\ell} = \{\hat{\boldsymbol{\theta}}_{y,\ell}, b_{2:j,\ell}\}$ with $b_{1:j,\ell}$ being the optimization variables.

where $\boldsymbol{\theta}$ denotes the set containing all the unknown parameters, i.e.

$$\boldsymbol{\theta} = [\boldsymbol{\theta}_1^T\ \ldots\ \boldsymbol{\theta}_d^T]^T \tag{14}$$

Regrettably, the resulting minimization will be both high-dimensional and multimodal, necessitating an accurate initial estimate of $\boldsymbol{\theta}$ to allow for a feasible estimator. In order to form such an initial estimate, we propose a relaxation-based (greedy) estimation scheme which recursively forms an approximative estimate of one mode at a time.

This is done by initially assuming that the signal only contains a single mode, i.e., that $d = 1$. Under this assumption, the parameters detailing this single mode are estimated as detailed below. Then, after this has been done, the found mode is removed from the measured signal, and a second mode is estimated from the resulting residual, which is then in turn removed from the measured signal to allow for a re-estimation of the first mode. This procedure is repeated until no significant improvement or until the number of maximal iterations are reached. Thereafter a third mode is estimated, and the procedure is repeated, and so on. The resulting procedure is summarized in the INRS Algorithm, Part 1, where $x_d(t,\ell)$ is defined as the time-domain residual obtained when, if assuming that the signal contains d modes, all but the ℓth estimated mode have been removed from the down-sampled and discrete-time analytical version of the measured signal, i.e.

$$x_d(t,\ell) \triangleq x(t) - \sum_{k=1,k\neq\ell}^{d} z_k(t, \hat{\boldsymbol{\theta}}_k) \tag{15}$$

Thus, in each of the steps, the lth mode is estimated as if it is the only mode present in the measurement. To allow for an efficient estimate, the polynomial attenuation of the mode is initially neglected, treating the examined residual signal, $x_d(t,\ell)$, for simplicity here termed $y(t)$, as formed by only a single mode with constant attenuation, such that

$$y(t) = y_0(t, \boldsymbol{\theta}_y) + v(t) \tag{16}$$

$$y(t) = \rho e^{-b_1 t} \exp\left\{ i \sum_{m=0}^{M} a_m t^m \right\} + v(t) \tag{17}$$

where ρ, b_1 and a_m, $m = 0, \ldots M$ denote the amplitude, constant damping and phase coefficients, respectively, for mode ℓ assuming totally d modes in the signal. $\boldsymbol{\theta}_y$ contain the unknown parameters detailing $y_0(t, \boldsymbol{\theta}_y)$, i.e.

$$\boldsymbol{\theta}_y = [\rho\ \ a_0\ \ b_1\ \ a_1\ \ \ldots\ \ a_M]^T \tag{18}$$

$$\boldsymbol{\theta}_y = [\rho\ \ a_0\ \ \boldsymbol{\theta}_{b_1,\mathbf{a}}^T]^T \tag{19}$$

and where $v(t)$ denotes a corrupting term containing the additive noise and the parts of the examined signal that are not captured by the first term in (17). We may thus estimate the parameters detailing the examined mode using LS as

$$\hat{\boldsymbol{\theta}}_y = \arg \min_{\boldsymbol{\theta}_y} \sum_{t=1}^{N} |y(t) - y_0(t, \boldsymbol{\theta}_y)|^2 \tag{20}$$

$$\hat{\boldsymbol{\theta}}_y = \arg \min_{\boldsymbol{\theta}_y} \|\mathbf{y}_T - \eta \mathbf{b}_{b_1,\mathbf{a}}\|_2^2 \tag{21}$$

where $\eta = \rho e^{i a_0}$, and

$$\mathbf{y}_T = [y(1)\ \ \ldots\ \ y(T)]^T \tag{22}$$

$$\mathbf{b}_{b_1,\mathbf{a}} = \begin{bmatrix} e^{b_1 + i(a_1 + \ldots + a_m)} \\ \ldots \\ e^{b_1 T + i(a_1 T + \ldots + a_m T^m)} \end{bmatrix} \tag{23}$$

implying that (see, e.g., [36], p. 157–9)

$$\hat{\boldsymbol{\theta}}_{b_1,\mathbf{a}} = \arg\max_{\boldsymbol{\theta}_{b_1,\mathbf{a}}} \gamma_{b_1}^{-1}(\mathbf{y}_T^* \mathbf{b}_{b_1,\mathbf{a}})(\mathbf{b}_{b_1,\mathbf{a}}^* \mathbf{y}_T) \tag{24}$$

where

$$\gamma_{b_1} = \sum_{t=1}^{T} e^{2b_1 t} = e^{2b_1} \frac{1-e^{2b_1 T}}{1-e^{2b_1}} \tag{25}$$

which, using $\hat{\boldsymbol{\theta}}_{b_1,\mathbf{a}}$, yields

$$\hat{\eta} = \gamma_{b_1}^{-1} \mathbf{b}_{b_1,\mathbf{a}}^* \mathbf{y}_T \tag{26}$$

and where the maximization in (24) may be formed, for instance, by a gradient search, e.g., using a method such as the one proposed in [37], with initial value a_1 set to the peak resonance frequency in the FFT, and the remaining parameters in $\boldsymbol{\theta}_{b_1,\mathbf{a}}$ set to initial value zero.

Finally, the parameters that are found are re-estimated using an LS fitting of $y(t)$ with the model $y_0(t,\boldsymbol{\theta}_y)$, wherein $\boldsymbol{\theta}_y$ is initialized to the found initial estimates, thereby allowing for an accurate initialization of the resulting gradient search. The overall INRS algorithm then proceeds to remove the found mode and re-estimate each of the assumed modes in the recursive fashion detailed in Algorithm 1. A practical convergence criteria for the iteration step is given by the normalized residual norm, defined as r, see Algorithm 1, line 9. After the iteration step, the algorithm add one extra mode if $\ell < d$, however, if the estimated peaks are to close, i.e., if $|a_{k_1,1} - a_{k_2,1}| < \epsilon_2$, $k_1 \neq k_2$, or if any of the estimated peaks are too close to zero $a_{k_1,1} < \epsilon_3$, $k_1 = 1,\ldots d$, the algorithm returns the estimated parameters assuming $\ell - 1$ modes in the signal. The first criterion assures that we do not model the same mode twice (which might happen if at least one of the assumed modes are very weak compared to the strongest peak), whereas the second criterion is needed to assure that we do not model the very weak frequency peak close to zero, which is an artefact from the applied wall filter. Before adding the polynomial attenuation, the resulting estimates of modes with constant attenuation are optimized simultaneously given the complex valued signal $x(t)$, see line 17 in Algorithm 1. The remaining polynomial attenuation coefficients of the modes are then estimated iteratively in an LS fitting of the signal $x(t)$ with the full model of all d modes, $\sum_{k=1}^{d} z_k(t,\boldsymbol{\theta}_k)$, where $\boldsymbol{\theta}$ is initialized to the parameter estimates found from the relaxation-based algorithm and with the initial value for the damping coefficients being set to zero, as described in Algorithm 2. A gradient search over all damping parameters detailing mode ℓ is then performed, see line 5. The new estimates are then re-used as initial values in the next LS fitting, sequentially adding additional damping coefficients for the considered mode in each step. Here, we perform these steps only for the strongest mode, although, if of interest, one could of course apply this kind of estimation procedure on all modes. Finally, when all damping coefficients have been added, a gradient search over all parameters in the model is performed with initial values obtained from the process described above, as described by the last line in Algorithm 2.

Table 2
The examined models of the phase and attenuation polynomials of the studied modes $f_{(2,1)}$, $f_{(0,1)}$ and $f_{(3,1)}$ (k=1, 2 and 3, respectively). Here, P_k and Q_k are the polynomial order of the phase and attenuation in the model, respectively.

Model	$f_{(2,1)}$		$f_{(0,1)}$		$f_{(3,1)}$	
	Q_1	P_1	Q_2	P_2	Q_3	P_3
1	1	1	1	1	1	1
2	2	1	2	1	2	1
3	2	1	3	1	2	1
4	2	1	4	1	2	1
5	2	1	3	2	2	1
6	2	1	3	3	2	1
7	2	1	3	4	2	1

5. Model evaluation

In order to determine appropriate polynomial orders for the examined modes, we proceed to examine the achievable accuracy of the model for varying polynomial orders, concluding that for $f_{(2,1)}$ and $f_{(3,1)}$, it is sufficient to use only low order polynomials, whereas the modeling of the dominating mode, $f_{(0,1)}$, is improved by allowing for a more detailed structure. These conclusions are found by examining the variance of the resulting residuals, estimated as

$$\hat{\sigma}_u^2 = \frac{1}{T-1} \sum_{t=1}^{T} \left[x(t) - \sum_{k=1}^{d} z_k(t,\hat{\boldsymbol{\theta}}_k) \right]^2 \tag{27}$$

where the model orders have been selected according to the examined model. Note that an improved model will result in a reduced residual variance, due to the larger extent of data that can be explained by the model. However, adding new parameters that does not significantly reduce the residual may result in over-fitting. For this reason, the analysis of the variance reduction is crucial for deciding on proper model orders. Table 2 details the examined models; here, the first model describes the modes as simple exponentially decaying sinusoids (linear response). Model 2 includes also a second order phase polynomial, enabling the modeling of the linear frequency change of the resonance frequencies with time. Model 3 further includes an additional phase coefficient to the dominant vibrational mode, $f_{(0,1)}$, permitting for the modeling of a quadratic time dependence on the resonance

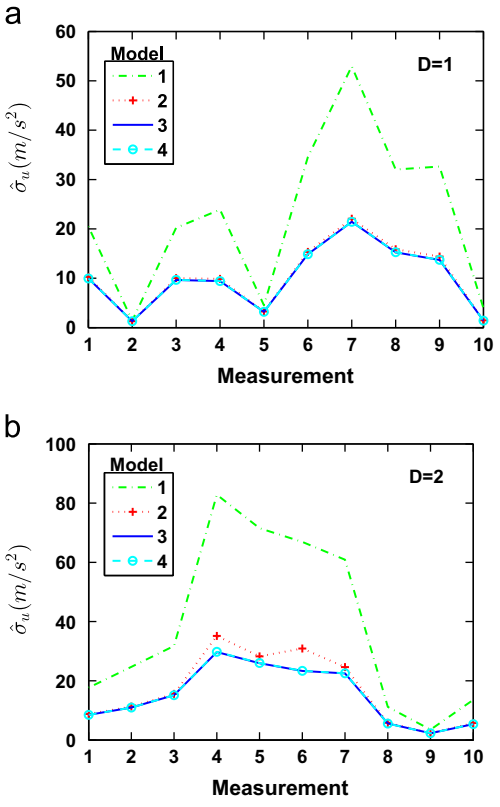

Fig. 4. Estimated residual standard deviations for the 10 measurements of the damage levels (a) D=1, and (b) D=2 for the initial four models.

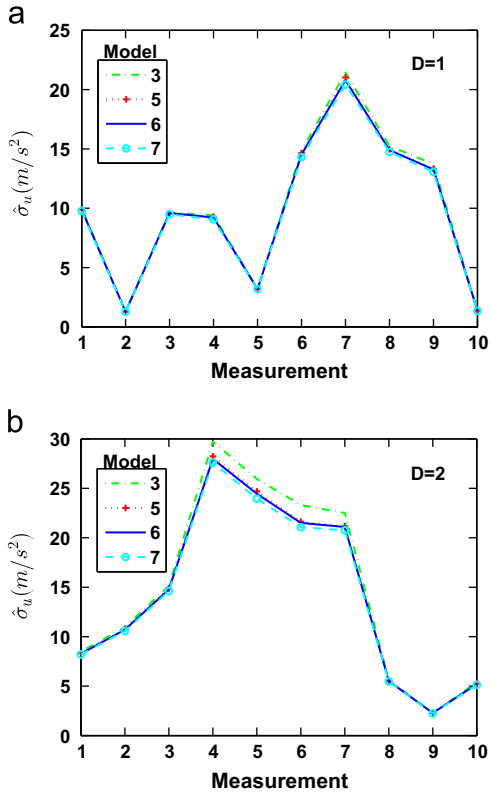

Fig. 5. Estimated residual standard deviations for the ten measurements of the damage levels (a) $D=1$, and (b) $D=2$ for models 3, 5, 6, and 7.

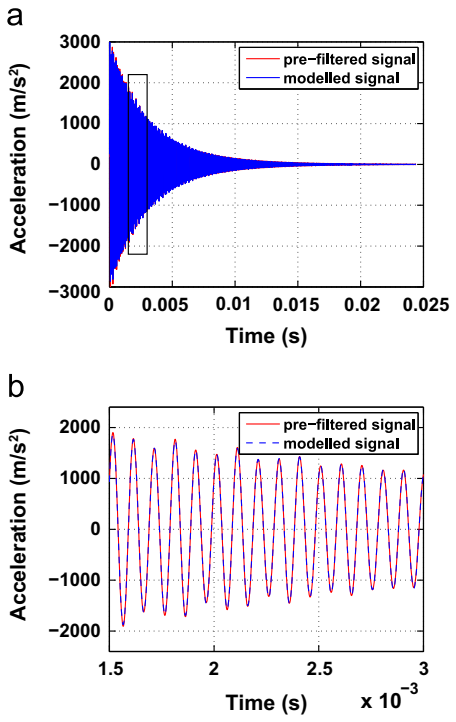

Fig. 6. The pre-filtered and modeled signal of a concrete sample with damage level $D=2$, shown in (a) the time-domain, and (b) zoomed version.

frequency of the mode. Similarly, model 4 includes a further phase coefficient to allow also for cubic frequency dependencies. In all these models, the attenuation is modeled using only a first order polynomial. Fig. 4 shows the estimated residual standard deviation for the ten measurements of damage levels $D=1$ and $D=2$. The

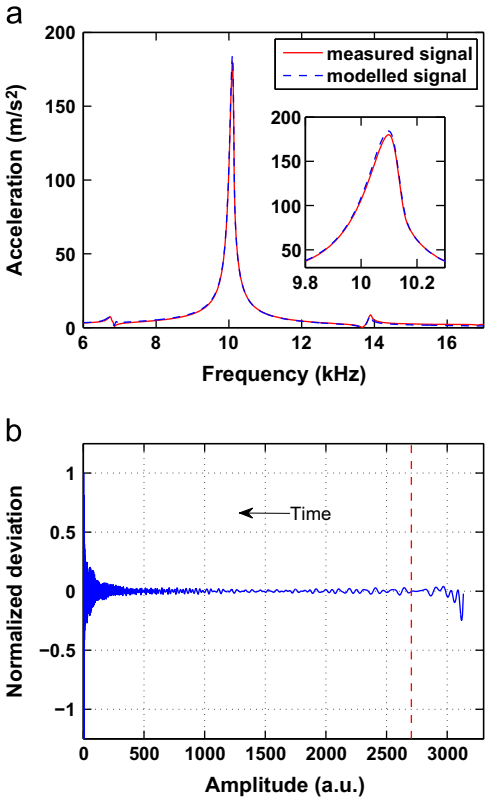

Fig. 7. (a) The measured signal and modeled signal of a concrete sample with damage level $D=2$, shown in frequency domain. A zoomed version of the dominant mode is given separately. (b) The normalized deviation versus instantaneous acceleration. The dashed line illustrates the higher acceleration limit for where we consider the model trustful.

residual standard deviations for damage level $D=3$ behave similar to the ones of $D=2$.

We see that the modeling is clearly improved when the frequency is allowed to vary linear with time (model 2), notably improving with the successively refining of the model from model 1 to model 3. It may further be noted that including the cubic dependency allowed for in model 4 does not notably improve the modeling. We therefore conclude that a reasonable model allows for the quadratic time dependency on the dominant vibrational mode, $f_{(0,1)}$, whereas it is sufficient to allow for a linear time dependency for the weaker modes, $f_{(2,1)}$ and $f_{(3,1)}$.

Proceeding to examine the attenuation model, we fix the polynomial phase orders as found above, i.e., using model 3, while instead extending models 5–7 to allow for a successively growing attenuation polynomial of the dominant mode. The resulting residual standard deviations for the examined measurements may be seen in Fig. 5, from which it may be noted that a first order attenuation is sufficient for sample of damage level $D=1$, whereas for damage level $D=2$, a second order attenuation is needed. However, allowing for a third or fourth order attenuation does not notably reduce the residual standard deviation. Therefore, we conclude that model 5 seems to be preferable for the examined measurements, and proceed to use it in the following evaluation. We note that if including other forms of substances in the experiment, or if notably changing the model setup, it may be beneficial to again perform a model order analysis such as the one above. However, for similar experiments and substances, no further model order analysis is needed, and the found model orders may be used directly.

Figs. 6 and 7 illustrate typical modeling results, here shown for a sample with damage level $D=2$. Fig. 6(a) shows the measured

and pre-filtered (real-valued) signal as compared to the resulting model signal using the estimated parameters, and Fig. 6(b) shows a zoomed part of the time domain signal, marked with a rectangle in Fig. 6(a). As is clear from the figures, the model fits the signal so closely so that it is difficult to distinguish between the two signals. This can also be seen in Fig. 7(a), showing the measured and modeled spectra. The subplot in Fig. 7(a) shows the dominant peak in more detail. If examined closely, it may be noted that the modeled signal has a slightly higher magnitude as compared with the measured signal. The normalized difference between the measured and modeled signal, in the time domain, is shown in Fig. 7(b), clearly illustrating the small deviation between the two signals. Here, to better illustrate the relative error, the difference between the signals is normalized with the amplitude of the envelope of the modeled signal; we term this the normalized deviation. The successively increase of the normalized deviation with decreasing acceleration of the signal is a consequence from the LS fitting, which penalizes model deviations in accordance with the signal amplitude, therefore emphasizing a better fit for the larger amplitudes at the cost of a worse fit for smaller amplitudes; the algorithm has been design to behave in this way as the non-linearity properties will be more pronounced for larger strain amplitudes. The model deviation observed for accelerations larger than 2700 m/s^2 is probably a consequence from the applied bandpass filter, which influences mainly the L first time elements in the model, where $L=228$ is the length of the filter.

6. Results and discussion

The measured data is first analyzed using the NIRAS method, where multiple signals obtained from different impacts with different strengths are compared for each damage state. The

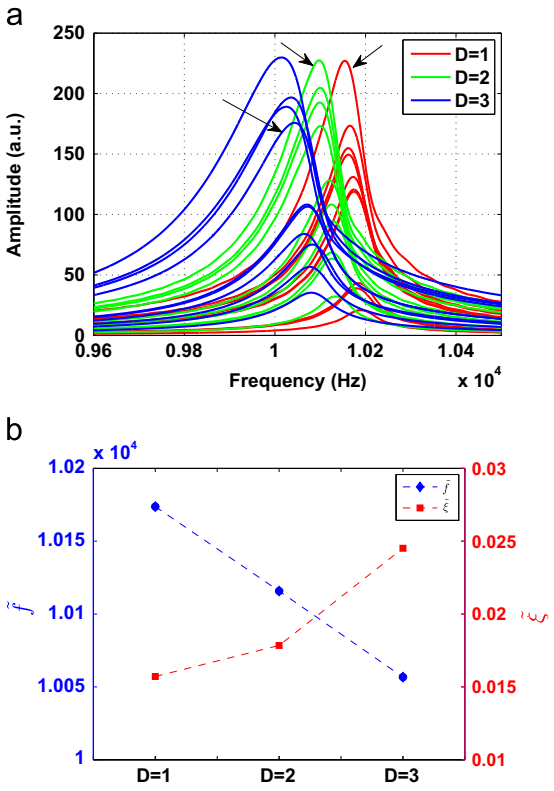

Fig. 8. (a) Data from each damage level, $D=1$, $D=2$ and $D=3$, illustrated in frequency domain. (b) Peak frequency and peak attenuation for the three signals marked with arrows in (a).

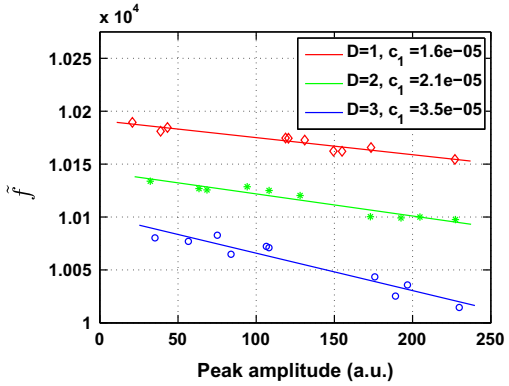

Fig. 9. Result from NIRAS. Normalized peak frequency shift as a function of the peak amplitude. c_1 is the hysteresis parameter obtained from a linear fit.

Fourier transformed data set, including 10 measurements with different impact strength from each damage state, is illustrated in Fig. 8(a). Here, the linear effect is clearly seen in terms of a downshift of frequency with increased damage level. In Fig. 8(b), the peak frequency, $\tilde{f}$, and attenuation, $\tilde{\xi}$, are shown for three signals from different damage states, but with similar amplitude in time domain. These signals are the ones more closely analyzed with the INRS method further on. The peak attenuation has been computed as the inverse of the Q-factor; the peak frequency divided by the full width half maximum (FWHM) for the strongest mode, $f_{(0,1)}$. As expected from the conventional linear method [12,13], a decrease of peak frequency as well as an increase in peak attenuation with increased damage level of the material can be observed. Fig. 9 illustrates an analysis obtained with the nonlinear method NIRAS. Here, the peak frequency shift is studied versus the peak amplitude for the 10 impacts from each damage level. The hysteresis parameter c_1 is obtained from a linear fit of the data from the same damage level (see Eq. (5)). As expected, one can observe an increase in the hysteresis parameter with increased damage of the specimen. The hysteresis parameter c_2 is in a similar way obtained from a linear fit of the normalized attenuation shift (see Eq. (6)). Also the hysteresis parameter c_2 increases with enhanced damage, taking the values 1.2×10^{-3}, 2.2×10^{-3} and 2.6×10^{-3}, when the damage of the sample is successively increased. Similar to other NIRAS studies, the observed shift in frequency and attenuation appears to be linear over a dynamic range of about a factor 8 [19,14,20–23].

Next, we study the results obtained with the proposed INRS method. Recall that this method requires only one measurement from each damage state in order to quantify the nonlinearity. Signals from different damage states, but with similar acceleration range, have been chosen to avoid effects that may arise from different initial strain amplitudes. The modeled frequency, f, for resonance peak $f_{(0,1)}$, is shown in Fig. 10(a) as a function of the modeled instantaneous acceleration, for one measurement from each damage levels $D=1$, $D=2$, and $D=3$, respectively. The shown model values have been obtained using model 5 and the L initial elements of the signal, with L being the length of the band pass filter, have been removed, due to the higher normalized deviation at these elements arising from the filter process.

Fig. 10(b) shows the modeled normalized frequency for resonance peak $f_{(0,1)}$, where we have set the linear resonance parameters, f_0, as the frequency values at an instantaneous acceleration of 70 m/s^2, approximately corresponding to the maximum frequency value obtained for each signal, as illustrated with the dashed line in Fig. 10(a). For comparison we have added the NIRAS result shown in Fig. 9 to the INRS result in Fig. 10(b). The modeled attenuation and the normalized attenuation for the three signals are shown in Fig. 11,

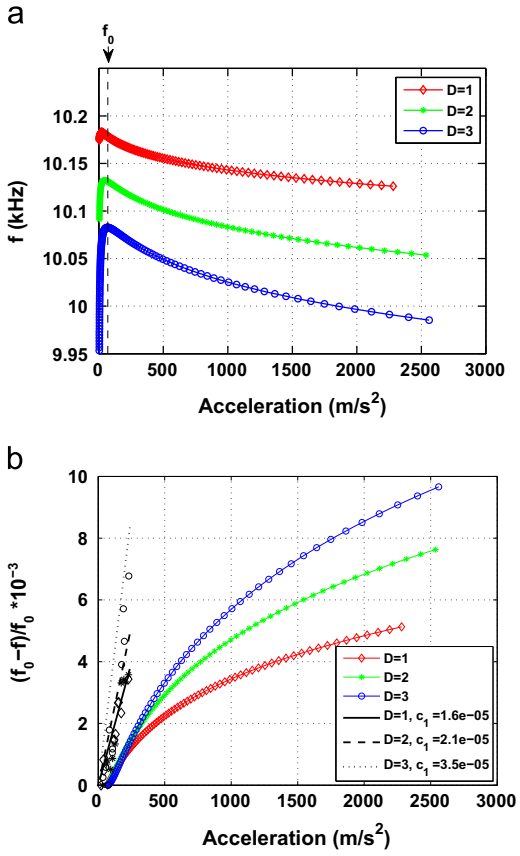

Fig. 10. (a) Modeled frequency versus modeled acceleration for concrete with different damage levels D. Here, f_0 is the linear frequency parameter. (b) Normalized frequency shift given by INRS and NIRAS (to the left).

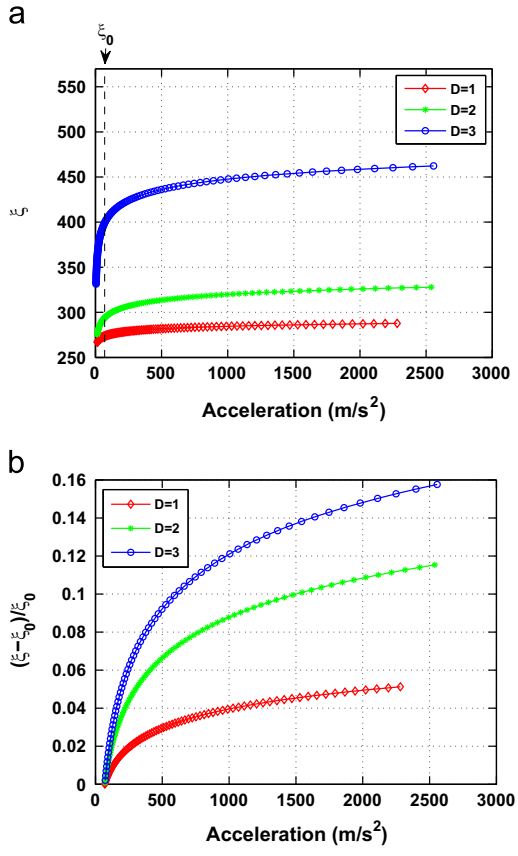

Fig. 11. (a) Modeled attenuation versus modeled acceleration for concrete with different damage levels D. Here, ξ_0 is the linear attenuation parameter. (b) Normalized attenuation shift.

where the linear attenuation parameters are the attenuation values at an instantaneous acceleration of 70 m/s^2, as shown in Fig. 11(a). We note that both the normalized frequency and normalized attenuation shifts increase with the degree of damage in the sample, which also agrees with previous studies, and with the NIRAS analysis. However, the non-linearity is now characterized over a noticeable wider dynamic range (70–2500 m/s^2) and a quadratic shift can be observed, which is expected over such a wide amplitude (or strain) range [30,31,27]. It is worth recalling that the amplitude here represents the true physical amplitude within the center of the sample and that the acceleration (normal component) is related to volumetric strain by a factor 10^{-9}. The results from INRS and NIRAS presented in Fig. 10(b) are thus not directly comparable, since NIRAS are based on the weighted average of the frequency and the amplitude content in the complete signal (peak amplitude from the FFT).

Fig. 12(a) shows the modeled frequency versus the modeled instantaneous acceleration for the 10 measurements made on the reference sample of steel. For the steel measurements, it was possible to extract and model the strongest mode alone. It is worth observing that the frequency resolution is very good (10^{-6}) and the measured acceleration is much smaller for the heavier steel sample, i.e., the highest acceleration in steel is 200 m/s^2, whereas the concrete measurements have accelerations approaching 2500 m/s^2. Note also that, in agreement with the modeling of the concrete, our modeling of steel indicates a decrease of frequency with decreasing acceleration for very low strain amplitudes (<70 m/s^2 for concrete and <10 m/s^2 for steel, i.e., below our chosen f_0 frequency). However, due to the way the model is designed (weight scaled with signal amplitude) and due to the low signal-to-noise in this acceleration ranges, it should be stressed that the normalized deviation is large here and the decreasing

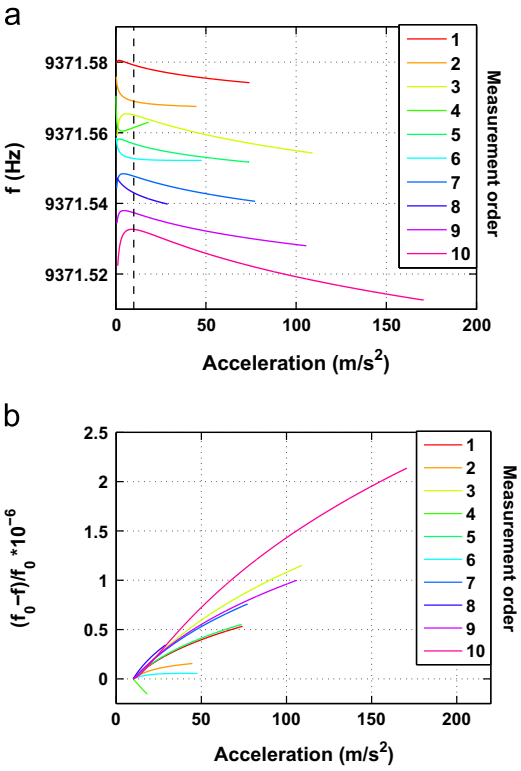

Fig. 12. (a) Estimated frequency versus estimated acceleration for 10 steel measurements. (b) Normalized frequency shift for steel.

frequencies are probably a best adjustment to the overall data. Given the unreliability of the estimation performance in this region, one should be careful to draw conclusions from the observed behavior at amplitudes below our chosen f_0. Fig. 12(b) shows the normalized frequency shift for steel, where the linear frequency parameter is again obtain as the values at the dashed line marked in Fig. 12(a), where the dashed line has been obtain from an analysis of the normalized deviation. We note that the normalized frequency shift for steel is of the order 10^{-6} in the acceleration range 100–150 m/s^2, whereas the normalized frequency shift for concrete in the same acceleration range is of the order 10^{-3}, emphasizing a notable weaker amplitude dependence on the reference sample steel, and that no major non-linear effects are present from the measurement system itself. In addition, the slow dynamic effect can be seen, i.e., the specimen has not returned to equilibrium, which results in a successively down-shift of the resonance frequency for each performed measurement [38]. This effect was not visible in the concrete results, due to the larger resonance shift with acceleration. It should be noted that the sensitivity of the measured resonance frequency at 10^{-6} is better than the 10^{-4} limit, which is often considered as the limit in NRUS measurements under normal experimental conditions [38].

Furthermore, we notice that measurements with larger initial strain amplitude show a stronger amplitude dependency on frequency. This effect was also observed in the concrete measurements where stronger amplitude dependency was observed for both frequency and attenuation. This is likely an effect of exceeding the threshold strain for non-linear and non-equilibrium effects (slow dynamics), as demonstrated by Pasqualini et al. [31]. The strain amplitude in this experiment is of the order 10^{-6}–10^{-8}.

7. Conclusions

In this work, we introduce a novel polynomial phase and attenuation model to describe the free reverberation from a standard impact resonance frequency test. Using the model, we introduce a relaxation-based least-squares fitting algorithm allowing for the reliable estimation of the model parameters, showing how the algorithm may be used to determine both the number of excited modes in the measured signal and the appropriate polynomial phase and attenuation orders for these modes. The proposed model allows continuous instantaneous true amplitude, frequency, and damping of each mode to be characterized as a function of time, allowing for detailed information of the non-linear parameters. The hysteretic material non-linearity can be characterized over a notably wider dynamic range compared to conventional NIRAS and NRS measurements. The INRS method only requires one single impact excitation and is fully compatible with the standard linear resonance test commonly used for concrete.

Acknowledgments

This work was supported in part by the Swedish Research Council (Grant no. 2011-5809), FORMAS (Grant no. 243-2012-1934), SBUF (Grant no. 12725), and Carl Trygger's foundation (Grant no. 13:193).

References

[1] Van Den Abeele K, De Visscher J. Damage assessment in reinforced concrete using spectral and temporal nonlinear vibration techniques. Cement Concr Res 2000;30(September):1453–64.
[2] Guyer RA, Johnson PA. Nonlinear mesoscopic elasticity: evidence for a new class of materials. Phys Today 1999(1):1–5.
[3] Van Den Abeele K, Carmeliet J, Cate JAT, Johnson PA. Nonlinear elastic wave spectroscopy (NEWS) techniques to discern material damage, Part II: single-mode nonlinear resonance acoustic spectroscopy. Res Nondestruct Eval 2000;12(1):31–42.
[4] Bentahar M, El Aqra H, El Guerjouma R, Griffa M, Scalerandi M. Hysteretic elasticity in damaged concrete: quantitative analysis of slow and fast dynamics. Phys Rev B 2006;73(January):014116.
[5] Eiras JN, Mondó J, Payá J, Kundu T, Popovics JS. Non-classical nonlinear feature extraction from standard resonance vibration data for damage detection. J Acoust Soc Am 2014;135(February):82–7.
[6] TenCate JA, Smith E, Guyer RA. Universal slow dynamics in granular solids. Phys Rev Lett 2000;85(July):1020–3.
[7] Kodjo AS, Rivard P, Cohen-Tenoudji F, Gallias J-L. Impact of the alkali-silica reaction products on slow dynamics behavior of concrete. Cement Concr Res 2011;41(April):422–8.
[8] Haller KCE, Hedberg CM. Method for monitoring slow dynamics recovery. Acoust Phys 2012;58(November):713–7.
[9] Van Den Abeele K, Johnson PA, Sutin A. Nonlinear elastic wave spectroscopy (NEWS) techniques to discern material damage, Part I: nonlinear wave modulation spectroscopy (NWMS). Res Nondestruct Eval 2000;12(1):17–30.
[10] Chen XJ, Kim J-Y, Kurtis KE, Qu J, Shen CW, Jacobs LJ. Characterization of progressive microcracking in Portland cement mortar using nonlinear ultrasonics. NDT & E Int 2008;41(March):112–8.
[11] Jhang K-Y. Nonlinear ultrasonic techniques for nondestructive assessment of micro damage in material: a review. Int J Precis Eng Manuf 2009;10(July):123–35.
[12] Martinček G. The determination of poisson's ratio and the dynamic modulus of elasticity from the frequencies of natural vibration in thick circular plates. J Sound Vib 1965;2(April):116–27.
[13] A.S. C215, Standard test method for fundamental transverse, longitudinal, and torsional resonant frequencies of concrete specimens; 2008.
[14] Leśnicki KJ, Kim J, Kurtis K, Jacobs LJ. Characterization of ASR damage in concrete using nonlinear impact resonance acoustic spectroscopy technique. NDT & E Int 2011;44(August):721–7.
[15] Payan C, Garnier V, Moysan J, Johnson PA. Applying nonlinear resonant ultrasound spectroscopy to improving thermal damage assessment in concrete. J Acoust Soc Am 2007;121(4):EL125.
[16] Sargolzahi M, Kodjo SA, Rivard P, Rhazi J. Effectiveness of nondestructive testing for the evaluation of alkali-silica reaction in concrete. Constr Build Mater 2010;24(August):1398–403.
[17] Idjimarene S, Bentahar M, El Guerjouma R, Scalerandi M. Effects of experimental configuration on the detection threshold of hysteretic elastic nonlinearity. Ultrasonics 2014;54(7):1861–7.
[18] Haller KCE, Hedberg CM. Constant strain frequency sweep measurements on granite rock. Phys Rev Lett 2008;100(February):068501.
[19] Chen J, Jayapalan AR, Kim J-Y, Kurtis KE, Jacobs LJ. Rapid evaluation of alkali-silica reactivity of aggregates using a nonlinear resonance spectroscopy technique. Cement Concr Res 2010;40(6):914–23.
[20] Chen J, Kim J-Y, Kurtis KE, Jacobs LJ. Theoretical and experimental study of the nonlinear resonance vibration of cementitious materials with an application to damage characterization. J Acoust Soc Am 2011;130(November):2728–37.
[21] Leśnicki KJ, Kim J-Y, Kurtis KE, Jacobs LJ. Assessment of alkali-silica reaction damage through quantification of concrete nonlinearity. Mater Struct 2012;46(December):497–509.
[22] Bouchaala F, Payan C, Garnier V, Balayssac JP. Carbonation assessment in concrete by nonlinear ultrasound. Cement Concr Res 2011;41(May):557–9.
[23] Eiras JN, Kundu T, Bonilla M, Payá J. Nondestructive monitoring of ageing of alkali resistant glass fiber reinforced cement (GRC). J Nondestruct Eval 2013;32(June):300–14.
[24] Ryden N. Resonant frequency testing of cylindrical asphalt samples. Eur J Environ Civil Eng 2011;15(4):587–600.
[25] Haach VG, Carrazedo R, Oliveira LMF, Corrêa MRS. Application of acoustic tests to mechanical characterization of masonry mortars. NDT & E Int 2013;59(October):18–24.
[26] Payan C, Ulrich TJ, Bas PYL, Saleh T, Guimaraes M. Quantitative linear and nonlinear resonance inspection techniques and analysis for material characterization: application to concrete thermal damage. J Acoust Soc Am 2014;136(2):537–46.
[27] Mendelsohn DA, Pecorari C. Nonlinear free vibration of a beam with hysteretic damage. J Sound Vib 2013;332:378–90.
[28] Abeele KVD, Bas PYL, Damme BV, Katkowski T. Quantification of material nonlinearity in relation to microdamage density using nonlinear reverberation spectroscopy: experimental and theoretical study. J Acoust Soc Am 2009;126:963.
[29] Winkler K, Nur A, Gladwin M. Friction and seismic attenuation in rocks. Nature 1979;277(February):528–31.
[30] Van Den Abeele K. Multi-mode nonlinear resonance ultrasound spectroscopy for defect imaging: an analytical approach for the one-dimensional case. J Acoust Soc Am 2007;122(July):73–90.
[31] Pasqualini D, Heitmann K, TenCate JA, Habib S, Higdon D, Johnson PA. Nonequilibrium and nonlinear dynamics in Berea and Fontainebleau sandstones: low-strain regime. J Geophys Res 2007;112(January):B01204.
[32] Graff KF. Wave motion in elastic solids. Dover Publications; 1991. ISBN-10: 0486667456, 13: 978-0486667454.
[33] Comsol. User's guide. Version 4.3 by COMSOL AB 2013, ⟨http://www.comsol.com/⟩ (date last viewed 12/1/12).
[34] Dahlén U. Damage identification in concrete using impact non-linear reverberation spectroscopy [Master's thesis]. Lund University; 2013.
[35] Marple SL. Computing the discrete-time analytic signal via FFT. IEEE Trans Signal Process 1999;47(September):2600–3.

[36] Stoica P, Moses R. Spectral analysis of signals. Upper Saddle River, NJ: Prentice-Hall; 2005.
[37] Lagarias JC, Reeds JA, Wright MH, Wright PE. Convergence properties of the Nelder–Mead simplex method in low dimensions. SIAM J Optim 1998;9:112–47.
[38] Haupert S, Renaud G, Rivière J, Talmant M, Johnson PA, Laugier P. High-accuracy acoustic detection of nonclassical component of material nonlinearity. J Acoust Soc Am 2011;130(November):2654–61.